**Astronomy
&
Astrophysics**

Deciphering the ultra-steep-spectrum diffuse radio sources discovered in the cool-core cluster Abell 980

Sameer Salunkhe[1], Surajit Paul[1], Gopal Krishna[2], Satish Sonkamble[3], and Shubham Bhagat[4]

[1] Department of Physics, Savitribai Phule Pune University, Pune 411007, India
  e-mail: `surajit@physics.unipune.ac.in`; `sameer@physics.unipune.ac.in`
[2] UM-DAE Centre for Excellence in Basic Sciences, University of Mumbai, Vidyanagari, Mumbai 400098, India
[3] INAF – Padova Astronomical Observatory, Vicolo dell'Osservatorio 5, 35122 Padova, Italy
[4] Thüringer Landessternwarte, Sternwarte 5, 07778 Tautenburg, Germany

ABSTRACT

Clusters of galaxies are excellent laboratories for studying recurring nuclear activity in galactic nuclei since their hot gaseous medium can vastly prolong the detectability of their radio lobes via better confinement. We report here a multi-band study of the sparsely studied galaxy cluster Abell 980, based on our analysis of *Chandra* X-ray data and GMRT (150 and 325 MHz) and EVLA (1.5 GHz) radio archival data, revealing an unusually rich phenomenology. It is shown to be a quasi-relaxed cluster with a cool core ($T \sim 4.2$ keV) surrounded by a hot and extensive intracluster medium (ICM) at $T \sim 6.8$ keV. The radio emission shows a rich diversity, having (i) two large diffuse sources of ultra-steep spectrum (USS) extending to opposite extremities of the ICM, each associated with an X-ray brightness discontinuity (cold front); (ii) a bright radio-double of size ~55 kpc coinciding with the central BCG; and (iii) a diffuse radio source, likely a mini-halo of size ~110 kpc around the BCG which possesses a huge ellipsoidal stellar halo of extent ~80 kpc. The association of cold fronts with two highly aged (~260 Myr) USS sources in a cool-core cluster makes it a very rare system. These USS sources are probably radio lobes from a previous episode of jet activity in the BCG, driven buoyantly towards the outskirts of the X-ray halo, thereby creating the cold fronts. A deeper radio image of this cluster may provide a rare opportunity to verify the recently proposed alternative model which explains radio mini-haloes as the aggregate radio emission from Type Ia supernova remnant occurring in the giant stellar halo extended across the cluster core.

Key words. radiation mechanisms: general – galaxies: clusters: individual: Abell 980 – radio continuum: galaxies –
X-rays: galaxies: clusters

1. Introduction

Clusters of galaxies are the natural habitat of diffuse steep-spectrum radio sources ($\alpha < -1.2$), usually identified as the quasi-confined relic lobes of once active radio galaxies (Baldwin & Scott 1973; Murgia et al. 2011; Godfrey et al. 2017). Detecting these sources, especially their ultra-steep-spectrum (USS) subset, requires (low-frequency) radio imaging with high sensitivity and a dynamic range at a fairly high spatial resolution. One signpost of such relic lobes are the 'cavities' sometimes detected in the X-ray images of galaxy clusters and groups (e.g., McNamara & Nulsen 2007). Their radio detection is facilitated by the brightness enhancement resulting from adiabatic compression by a passing shock wave usually launched during the merger(s) of the host cluster with another galaxy group or cluster (Enßlin & Gopal-Krishna 2001). Such 'radio phoenixes' are thus not expected to be found in cool-core clusters. On the other hand, such clusters sometimes exhibit radio mini-haloes, the diffuse radio sources of steep spectrum extending to ~100 kpc around the brightest cluster galaxy (BCG) (e.g., Giacintucci et al. 2019). Although studies of USS radio sources in clusters have now received a big boost with the availability of dedicated low-frequency radio telescopes, such as the LOw Frequency ARray (LOFAR) and the upgraded Giant Metrewave Radio Telescope (uGMRT; e.g., Savini et al. 2018), archival research continues to surprise us by revealing extraordinary objects, and here we report one such finding in the comparatively low-mass cluster Abell 980.

Abell 980 (A980; RXC J1022.5+5006) at $z = 0.1582$ (Lebedev & Lebedeva 1991), has an SZ mass $M_{500}^{SZ} = 4.73_{-0.32}^{+0.29} \times 10^{14}\,M_\odot$ (Planck Collaboration XIII 2016), a high X-ray luminosity ($L_X = 7.1 \times 10^{44}$ erg s^{-1}), and an average ICM temperature (7.1 keV; Ebeling et al. 1996). By processing the WENSS survey data, with a resolution of 54″ at 330 MHz, Rudnick & Lemmerman (2009) showed that A980 has a luminosity $P_{330\,MHz} = 5.6 \pm 1.3 \times 10^{24}$ W Hz^{-1} at 330 MHz, and that some marginally resolved faint emission underlies a dominant radio peak.

This paper reports the discovery of a rich assembly of steep to ultra-steep-spectrum radio sources in A980 by analysing the archival data from GMRT (150 and 325 MHz), EVLA (1.5 GHz), and *Chandra* (soft X-rays). Section 2 describes the data analysis, the results of which are summarized in Sect. 3 and discussed in Sect. 4, followed by our main conclusions given in Sect. 5. A Lambda cold dark matter (ΛCDM) cosmology is assumed with parameters $H_0 = 70$ km s^{-1} Mpc^{-1}, $\Omega_M = 0.3$, $\Omega_\Lambda = 0.7$. The physical scale for the images is 2.73 kpc arcsec^{-1}.

2. Observations and data reduction

2.1. Analysis of the radio data

We analysed a total of 100 min (150 MHz) and 314 min (325 MHz) of on-source GMRT archival data (Project: ddtB020 and 17_073) from RR and LL correlations using the Source Peeling and Atmospheric Modeling (SPAM) pipeline

Table 1. Parameters of the radio images.

Frequency (MHz)	Robust (briggs)	uv-taper ($k\lambda$)	FWHM (in ″; PA in °)	rms (μJy beam^{-1})
150	−0.5	8	$33 \times 21; 59$	5500
325	Uniform	–	$6.7 \times 5.7; 5^h$	140
	−2	–	$8.2 \times 7.3; 7^m$	100
	0	10	$19 \times 16; 61^l$	215
1500	−2	–	$2.8 \times 2.5; 63^h$	30
	0	10	$9.0 \times 8.7; 31^l$	25

Notes. Resolutions: h – high, m – medium, l – low.

(for details, see Intema et al. 2017). This pipeline takes care of direction-dependent variations in visibility amplitude and phase across the field of view, due to the antenna beam pattern and the ionosphere. In the initial SPAM steps, the calibrator 3C48 was used for flux density and bandshape calibration. The available 56 min of EVLA L-band (1–2 GHz, B-array) data (Project: 15A-270 and 12A-019) from RR and LL correlations were imaged using the Common Astronomy Software Applications (CASA) calibration pipeline and performing several rounds of phase-only self-calibration and one amplitude and phase self-calibration. Images with multiple angular resolutions were made using the various weighting and uv-taper parameters listed in Table 1. The spectral index and error maps were produced using the IMMATH task of CASA following the standard relations and taking the data from different frequencies (Appendix A.1).

Since the radio emission from A980 is found to consist of a diffuse source coinciding with the BCG and several discrete sources in the vicinity, an enhanced diffuse radio emission map was also generated by filtering the discrete source contributions. We broadly followed the procedure given in van Weeren et al. (2014). Firstly, an image of the discrete sources was made by only using uv spacing $>3\,k\lambda$. The corresponding visibilities were then subtracted from the observed UV data and the final low-resolution image was made setting the Briggs weighting, robust = 0, and a uv-taper of $10\,k\lambda$.

All measurements on the images were carried out using the CASA viewer. The flux densities (S) were measured within the 3σ isophotes of a given source and the errors (σ_S) were calculated as $\sigma_S = \sqrt{(0.1S)^2 + N\sigma^2 + \sigma_{sub}^2}$, where N is the number of beams across the diffuse emission, $0.1S$ is assumed to be the error due to calibration uncertainties, and σ_{sub} is the uncertainty arising from the compact source subtraction procedure (applied to the point-source-subtracted maps only).

2.2. Analysis of the X-ray data

The level-1 event file of A980 from the *Chandra* data archive (14 ks; ObsID 15105) was reprocessed following the standard data reduction routine of CIAO[1] 4.11 and employing the latest calibration files CALDB 4.8.3. Events were screened for cosmic rays using the ASCA grades, and were reprocessed by applying the most up-to-date corrections for the time-dependent gain change, charge transfer inefficiency, and degraded ACIS detector quantum efficiency. Periods of high background flares exceeding 20% of the mean background count rate were identified and removed using the lc_sigma_clip algorithm. This yielded 13.5 ks of net exposure time. The standard blank-sky
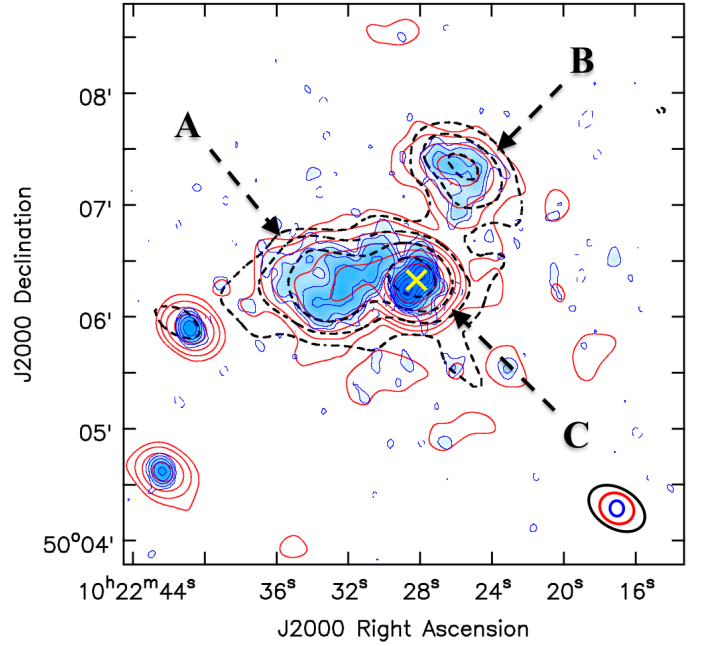
---

[1] http://cxc.harvard.edu/ciao

Fig. 1. GMRT 325 MHz medium-resolution image (in blue, contours drawn at $\pm 3, 6, 12, \ldots \times \sigma$; $\sigma = 100\,\mu$Jy beam^{-1}) overplotted with the 325 MHz low-resolution map (red contours) at $\pm 3, 6, 12, \ldots \times \sigma$ ($\sigma = 215\,\mu$Jy beam^{-1}). The 150 MHz GMRT map is shown with black dashed contours drawn at $\pm 3, 6, 12, \ldots \times \sigma$ ($\sigma = 5.5$ mJy beam^{-1}).

datasets[2] were processed and reprojected to the corresponding sky positions and normalized to match the count rate in the $10 - 12$ keV energy range. Point sources across the ACIS field, except the nucleus of A980, were identified using the CIAO tool wavdetect and removed (for details, see Sonkamble et al. 2015). Thereafter, exposure correction was applied on the cleaned X-ray image (i.e., free from point sources and flares), using the mono-energetic exposure map created at 1 keV.

3. Results

3.1. Radio properties

3.1.1. Radio structural properties of A980

In Fig. 1 the radio emission is concentrated in the regions, A, B, and C which encompasses the BCG (yellow cross). These sources are seen at all three of the radio frequencies, except B which is undetected at 1.5 GHz (see below).

Using the medium-resolution GMRT map at 325 MHz (see Fig. 1), the sizes of A and B were measured to be 190×170 kpc and 140×140 kpc, respectively. The 1.5 GHz VLA map (Fig. 2) detects only the emission associated with the BCG and the brighter parts of A. Unlike B, the sources A and C are not clearly separated in the GMRT 150 MHz map, but their flux densities can still be measured fairly accurately as 261 ± 26 mJy and 117 ± 12 mJy, respectively. Figure 2 shows that region C at 325 MHz and 1.5 GHz is comprised of (i) a double radio source of size ~ 20 arcsec at position angle PA = 135 deg, straddling a core which is seen only at 1.5 GHz and which coincides with the BCG, and (ii) an underlying faint and hence not so clearly imaged mini-halo candidate measuring 0.9 arcmin (north–south) (Fig. 2b and Table 2).
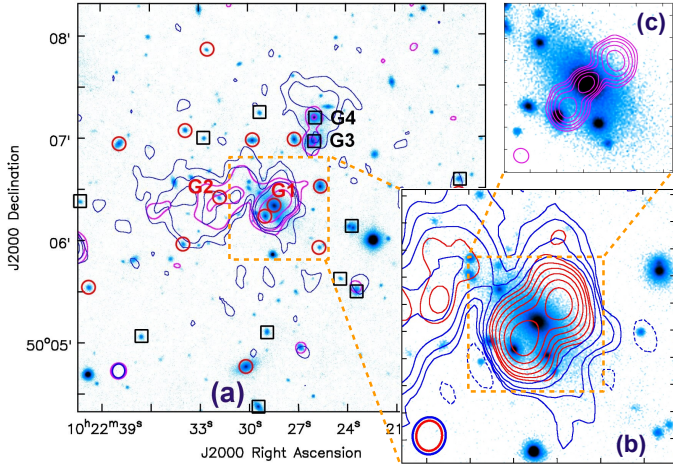
---

[2] http://cxc.harvard.edu/ciao/threads/acisbackground/

Fig. 2. Multi-band (radio-optical) overlays of cluster A980. *Panel a*: Pan-STARRS *i*-band optical image superimposed with the low-resolution VLA *L*-band map (magenta contours at $3, 9, 81 \times (\sigma = 25\,\mu\text{Jy beam}^{-1})$) and the 325 MHz medium-resolution GMRT map (blue contours at $3, 9, 27 \times (\sigma = 100\,\mu\text{Jy beam}^{-1})$). The cluster galaxies ($z = 0.1582 \pm 0.0035$; red circles) and foreground or background galaxies ($z < 0.1547$ or $z > 0.1617$; black squares) are shown within the field. The estimated redshift range ($\Delta z = 0.0035$) equivalent to the velocity dispersion ($v_{\text{rms}} = 1033\,\text{km s}^{-1}$) of the cluster (Rines et al. 2013). *Panel b*: contours (red) of the GMRT 325 MHz map with uniform weighting, plotted at $5, 10, 20, \ldots \times (\sigma = 140\,\mu\text{Jy beam}^{-1})$ and those with robust-2 setting (blue), plotted at $3, 6, 12, \ldots \times (\sigma = 100\,\mu\text{Jy beam})$. *Panel c*: high-resolution VLA *L*-band contours are plotted at $3, 6, 12, \ldots \times (\sigma = 30\,\mu\text{Jy beam}^{-1})$.

Table 2. Measured parameters of the main radio components.

Source	Flux density (mJy)			Spectral index	
	[150 MHz	325 MHz	1.5 GHz]	[α_{150}^{325}	α_{325}^{1500}]
A	261 ± 26	54.3 ± 5.5	1.4 ± 0.2	-2.0 ± 0.3	-2.4 ± 0.2
B	117 ± 12	20.4 ± 2.1	<0.89	-2.3 ± 0.3	<-2.1
C	281 ± 28	120 ± 12	13.8 ± 1.4	-1.1 ± 0.3	-1.4 ± 0.1

3.1.2. Radio spectral properties

For the entire complex seen in Fig. 1, the spectral index was computed, first by combining the GMRT 150 MHz and 325 MHz (low-resolution) maps, integrating within 3σ contours, yielding $\alpha_{150}^{325} = -1.56 \pm 0.25$. Furthermore, we combined the medium-resolution GMRT 325 MHz map with the low-resolution VLA map at 1.5 GHz (see Table 1), restricting the integration to within their overlapping portions, which gave $\alpha_{1500}^{325} = -1.49 \pm 0.13$. Spectral indices of the individual sources are given in Table 2, one of which is an upper limit, owing to the non-detection of B at 1.5 GHz (Fig. 2a). The spectra of both A and B remain very steep even at low frequencies, with $\alpha_{150}^{325} = -2.0 \pm 0.3$ for A and -2.3 ± 0.3 for B. This is highly reminiscent of relic radio sources (e.g., Murgia et al. 2011). Figure 3, displays the variation in α_{150}^{325} across the sources A and B; starting from ≈ -1.6 near the inner region adjacent to C, it steepens to ≈ -2.7 near their extremities. For both these USS sources, we estimated spectral ages since the cessation of energy input ($\sim 265 \pm 33$ Myr for A and $\sim 260 \pm 45$ Myr for B), following the procedure followed in Jamrozy et al. (2004) and adopting the JP model (details in Appendix A.3). The derived ages are lower limits since the spectral break frequency was taken to be 150 MHz, the lowest
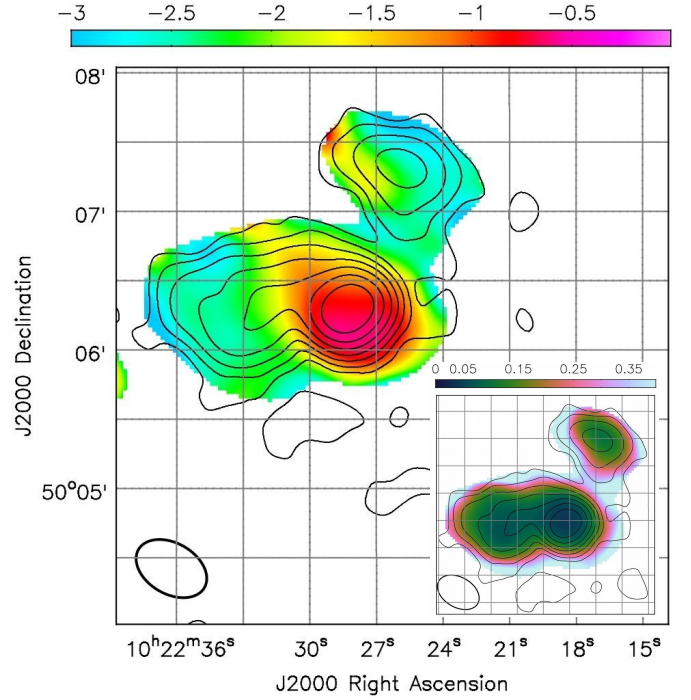

Fig. 3. GMRT spectral index and error (inset) maps (150–325 MHz) with beam size of $33'' \times 22''$, PA = 60°. The contour levels are same as in the low-resolution map at 325 MHz (Fig. 1).

observed frequency. The derived equipartition magnetic field for A and B are 2.6 µG and 3.2 µG, respectively. The small double source hosted by the BCG also shows a rather steep spectrum ($\alpha_{150}^{325} \gtrsim -1.1$ and $\alpha_{325}^{1500} = -1.3 \pm 0.1$) and its estimated spectral age is ~ 70 Myr.

3.2. X-ray properties

From the *Chandra* archives, we extracted the $0.5-8$ keV spectrum of the region within 150 arcsec, (408 kpc) of the X-ray peak, after excising the central 2 arcsec region at the peak associated with the nucleus of the double radio source within C, as well as other obvious point sources (details in Appendix B.1). Figure 4a presents the 5σ Gaussian-smoothed *Chandra* image ($0.5-3.0$ keV), revealing a roughly circular extended source. However, a few faint substructures and a mild elongation can be noticed towards the north-east of the X-ray peak (see Fig. 4a). For the ICM we estimate the best-fit global elemental abundance of $0.33 \pm 0.08\,Z_\odot$, a temperature (T) of 6.8 ± 0.4 keV, and an integrated $0.5-8$ keV luminosity of $5.9 \pm 0.1 \times 10^{44}$ erg s^{-1} (Appendix B.1). The radial surface-brightness profile, assuming a spherically symmetric ICM (see Fig. 4b; and Appendix B.2 for details), is well represented by a double β-model, showing a prominent core of high surface brightness. The best-fit model parameters are given in Table B.1.

3.2.1. The X-ray edges

As seen in Fig. 4a, the outer edges of the diffuse radio sources A and B (indicated by the cone-shaped sectors, in red) appear roughly aligned with the X-ray contours near the ICM outskirts. In the radial X-ray surface-brightness profiles for these sectors encompassing the radio sources A and B, we have detected discontinuities (Fig. 4c). To examine any change in conditions
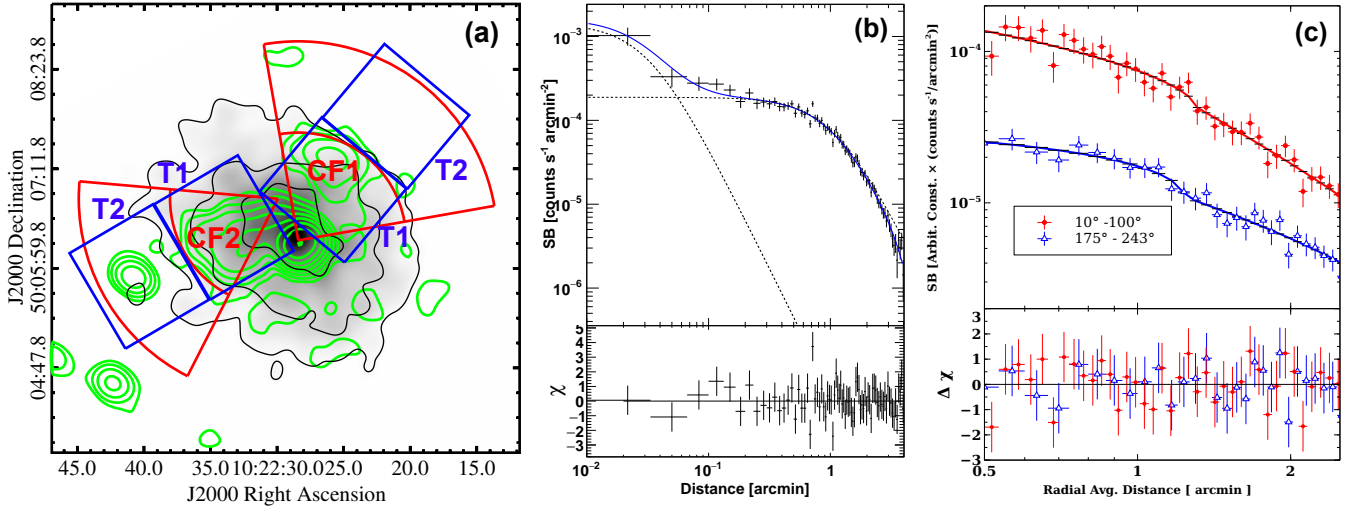
Fig. 4. Various X-ray properties of cluster A980. *Panel a*: *Chandra* X-ray map in gray and black contours, over-plotted with the GMRT 325 MHz (low-resolution) contours (green). The sectors (10°−100° (CF1) and 175°−243°(CF2)) along which sources B and A are extended, respectively, are marked as red cones. Blue boxes denote the pre- and post-cold-front regions (T_2 and T_1, respectively) (see text). *Panel b*: azimuthally averaged X-ray surface brightness (SB) profile, with the best-fit double β-model. The individual β-models are shown with dotted lines and the residuals are shown in the *bottom panel*. *Panel c*: SB profiles for the two conal sectors and the fitted broken power-law models are shown with red and blue curves, respectively.

Table 3. Properties of the cold fronts seen at A and B (details in Table B.2).

Conal sector	Radial position	Density enhancement factor	T_1 (keV)	T_2* (keV)	Temperature jump ($\Delta T = T_2$-T_1 (keV))	P_1 10^{-11} erg cm^{-3}	P_2 10^{-11} erg cm^{-3}
10°−100°(A)	1.30′	1.20 ± 0.12	5.77 ± 0.48	10.90 ± 3.33	5.13 ± 3.36	4.49 ± 0.40	5.38 ± 0.72
χ^2/d.o.f.	–	–	56.33/57	23.82/24	–	–	–
175°−243°(B)	1.32′	1.35 ± 0.15	5.53 ± 0.52	12.22 ± 3.87	6.69 ± 3.90	1.04 ± 0.10	1.03 ± 0.32
χ^2/d.o.f.	–	–	58.77/57	21.74/25	–	–	–

Notes. * – metallicity fixed to 0.33 $Z_\odot$ i.e., average metallicity of this cluster.

across these X-ray 'edges', we defined a pair of square regions (blue boxes) on opposite sides of each edge (Fig. 4a) and determined the electron density, temperature, and pressure within these boxes (see Appendix B.3 for the methodology). The deprojected electron density profile along sectors CF1 and CF2, as well as the temperature determined for the pairs of boxes, show significant change in values of density and temperature across the boxes. This indicates physical differences in the ICM on the two sides of the outer edge of both A and B (Fig. 4c and Table 3). In both cases the box on the inner side of the radio edge has a lower temperature ($T1$), whereas no significant change is seen in pressure (see Appendix B.3 and Table 3). This is strongly suggestive of a cold front for each of these two X-ray discontinuities. We also note a marginally significant radial increase in metallicity (0.59 ± 0.45) found across the cold front CF1.

3.2.2. The X-ray temperature map

A 2D temperature map was derived using the contour-binning algorithm by Sanders (2006). This algorithm generates a set of regions following the distribution of the surface brightness so that each region has nearly the same signal-to-noise ratio. A total of nine regions were thus delineated, each with a signal-to-noise ratio of 20 (~400 counts per bin) from the 0.5−3.0 keV image. We then extracted the X-ray spectrum for these regions and fitted with the model TBABS × APEC using the method described in

Appendix B.1. While fitting, we fixed the metallicity at 0.33 $Z_\odot$, the average metallicity of this cluster. The final map is shown in Fig. 5 overlaid with temperature values and corresponding uncertainties.

The temperature map reveals large spatial variations in T, indicating the presence of substructures. Although, the core is distinctly cool with a temperature $T = 4.2 \pm 0.6$ keV (size ~100 kpc), patches with temperature as high as $T \sim 12$ keV are seen immediately north-east of the cool core, roughly co-spatial with the few X-ray substructures mentioned in Sect. 3.2. Overall, the cluster ICM has a high average temperature of $T \sim 6.8$ keV, as found in the present analysis (Sect. 3.2).

4. Discussion

As we state in Sect. 3.1.1, the radio emission in A980 can be segregated into four main components: two large diffuse USS radio sources A and B, both having $\alpha \lesssim -2$, and a region C consisting of a smaller double radio source (~55 kpc) at the BCG and an underlying faint extended steep-spectrum radio source (~100 kpc). Below we outline some likely scenarios for their origin.

4.1. Episodic AGN activity and the relic radio lobes

In Figs. 1 and 2 it can be seen that the USS sources A and B are diffuse and moderately luminous (~3.7 × 10^{24} W Hz^{-1} and

$\sim 1.4 \times 10^{24}\,\mathrm{W\,Hz^{-1}}$ at 325 MHz, respectively), strongly reminiscent of relic lobes of radio galaxies that are no longer active (e.g., Jamrozy et al. 2008; Murgia et al. 2011; Godfrey et al. 2017). Galaxies G3 and G4 are seen close to B; however, their redshifts ($z = 0.149556$ and 0.152417) are significantly different from that of A980. Furthermore, each has its own barely resolved radio counterpart seen in the VLA *L*-band low-resolution map at 1.5 GHz (see Fig. 2a), with the spectrum ($\alpha \lesssim -1$; see Appendix A.1) of an active point-like radio source. Therefore, both these normal-spectrum radio sources are highly unlikely to be physically associated with the diffuse USS source B. The galaxy G2, which is centrally located within USS source A is undetected in the VLA-FIRST survey. Moreover, its apparent magnitude $m_r = 20.06 \pm 0.05$ (PANSTRASS-DR1, Chambers et al. 2016) corresponds to an absolute magnitude $M_r = -19.39 \pm 0.05$, at its redshift $z = 0.161662$. This is 3.4 mag under-luminous than the average absolute magnitude (-22.8 ± 0.5) of the ellipticals hosting radio galaxies at $z < 0.5$ (Sbarufatti et al. 2005), which makes it a very unlikely host of source A. Thus, there are no viable optical identifications for A and B as independent radio sources. This, together with the similar spectral ages of 265 Myr (A) and 260 Myr (B) (see Sect. 3.1.2) and the conspicuous radio extension of A towards B strongly suggest that the two USS sources are aged lobes of a common host galaxy.

Considering the absence of likely host galaxies for A and B and given that intermittent nuclear activity is a common feature of radio galaxies (e.g., Godfrey et al. 2017; Turner 2018), it seems quite plausible that A and B are aged remnants of a powerful double radio source created by the BCG (G1 in Fig. 2a) in its previous active phase, and that both have risen to the ICM outskirts due to buoyancy pressure, while remaining confined due to the thermal pressure of the hot ICM. Concurrently, the galaxy has drifted towards the cluster centre where it has entered a new active phase resulting in the small double source with an associated compact radio core (Figs. 2b and c). In the absence of a clear tracer of a jet axis in the available maps, we considered the line joining the outermost parts of the two old lobes as an approximate location of the radio axis from where the BCG (G1) would have to move a distance of about 100 kpc to arrive at its present location near the cluster centre. This postulated trajectory of the drift is the natural radial direction for the infall towards the cluster centre as inferred from the X-ray peak which has a very small offset ($\sim 2\,\mathrm{arcsec} = 5.5\,\mathrm{kpc}$) from the present location of the BCG. We note that in order to cover the (projected) distance of $\sim 100\,\mathrm{kpc}$ within the age of the two USS sources A and B created by it, the required drift velocity is $\sim 400\,\mathrm{km\,s^{-1}}$, which is not exceptional for BCGs (e.g., Sohn et al. 2020) in quasi-relaxed clusters and is certainly well within the observed velocity dispersions (1033 km s^{-1}) of the galaxies in this cluster (Rines et al. 2013).

4.2. Fossil radio lobes and the X-ray edges in the ICM

Discrete USS sources inside the cluster ICM can also be detectable when fossil radio lobes remaining from a past episode of jet activity in a cluster galaxy are subject to adiabatic compression caused by a passing shock wave from the cluster's merger with another galaxy cluster or group (Enßlin & Gopal-Krishna 2001). However, there is no evidence of a shock within the ICM of this cool-core cluster, particularly in the vicinity of the two USS sources (Fig. 4). Nonetheless, other imprints of the two USS radio lobes are discernible in this X-ray image, namely a discontinuity in the radial profile
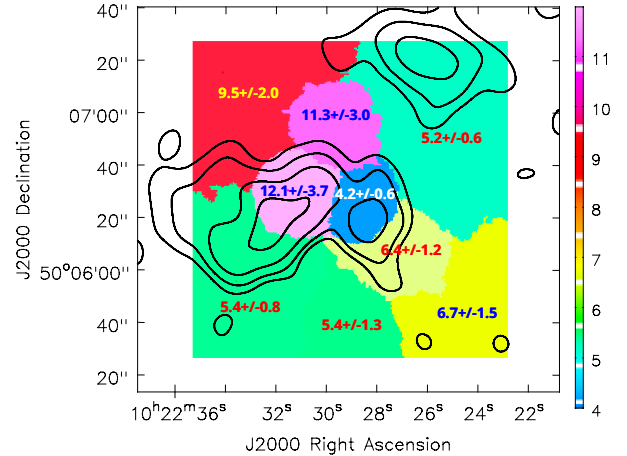

Fig. 5. *Chandra* X-ray temperature (keV) map overlaid with the radio contours (at $3, 6, 12, \ldots \times 250\,\mu\mathrm{Jy\,beam^{-1}}$) of the point-source-subtracted 325 MHz GMRT map.

of X-ray brightness (but not in pressure) along each lobe consistent with a cold front at the lobe's leading edge (Sect. 3.2.1). The distinct widening of both the remnant lobes near their outer edges would be consistent with this scenario. On the other hand, it is conceivable that a coherent magnetic field in the cold front caused the sharp outer edges of the lobes A and B, as inferred from the observed structure in A980, which resembles a 'double scythe' (Chibueze et al. 2021). Clearly, a credible detection of such a structure is sensitively dependent on the jet's orientation relative to the line of sight, which is poorly constrained in the present case. However, the non-detection of a compact radio component between A and B, and their diffuse appearance with an ultra-steep radio spectrum, together constitute a strong hint that currently there are no jets feeding either of these lobes.

A likely process giving rise to the cold fronts detected in A980 is the outward pressure exerted due to the buoyancy-driven, near-sonically moving relic lobes (Markevitch & Vikhlinin 2007). However, an alternative to the cold front scenario has been proposed for the case of NGC 507, the central galaxy of the Pisces cluster ($z = 0.01646$). Its *Chandra* image shows a prominent, sharp discontinuity in X-ray brightness (but only marginally in temperature) which is aligned with the outer edge of a radio lobe (Kraft et al. 2004). These authors have questioned the cold front description of this system in view of the sharpness and large magnitude of the brightness discontinuity, which however is not reflected in a temperature jump, and the lack of evidence for a radio lobe beyond the discontinuity that could have maintained a pressure balance. They interpret the brightness discontinuity to arise substantially from an elemental abundance gradient across it (see also Kempner & David 2004) and find a higher elemental abundance in the cooler low-entropy ICM within the cluster core, which has probably been entrained and transported outwards in the wake of the advancing radio lobes (see e.g., Heinz et al. 2003; Paul et al. 2020). A potential caveat from the present perspective is that this argument based on abundance gradient works much more robustly for low-temperature ICM ($T < 2\,\mathrm{keV}$) whose X-ray emissivity is high (Kraft et al. 2004).

4.3. Radio mini-halo in formation?

Our GMRT map of A980 at 325 MHz has revealed an extended diffuse radio source underlying the double radio source

associated with the BCG (Fig. 2b). It is seen more clearly in the point-source-subtracted version of that map (Fig. 5 and Sect. 2.1) where it is overlaid on the X-ray temperature map from our analysis of the *Chandra* data (Fig. 5 and Sect. 3.2.2). The diffuse radio source clearly overlaps the cool core, both having a size of ~100 kpc. For this source with diffuse morphology, we estimate a flux density of 11.5 ± 1.3 mJy at 325 MHz, which corresponds to a luminosity of $7.9 \pm 0.9 \times 10^{23}$ WHz^{-1} and a radio emissivity of $1.1 \pm 0.2 \times 10^{-40}$ ergs^{-1} cm^{-3} Hz^{-1} (see Appendix A.2). With a size of ~100 kpc (similar to the cool core) and a characteristic higher radio emissivity compared to giant radio haloes (Murgia et al. 2009), the diffuse source detected around the BCG, can plausibly be classified as a radio mini-halo (e.g., Giacintucci et al. 2019).

A popular mechanism for such sources invokes the re-acceleration of pre-existing low-energy electrons in the ICM by turbulence induced by gas-sloshing (Fujita et al. 2004; ZuHone et al. 2013). In the present case this could be caused by the postulated infall of the BCG (Sect. 4.1) or possibly by the minor mergers suggested by the X-ray substructures roughly co-spatial with high-temperature patches (see Sects. 3.2 and 3.2.2) towards the north-east of the BCG. It should be noted that a similar hot patch has been reported for the ICM of the cool-core cluster RX J1347.5−1145 (Gitti & Schindler 2004). Here, we recall an alternative mechanism, according to which radio mini-haloes represent aggregate radio output from Type Ia supernova remnant occurring in the stellar population distributed across the cluster core (Omar 2019). If true, this alternative mechanism would obviate the need for the turbulent re-acceleration of relativistic particles in order to create a radio mini-halo within the inner ICM. The mini-halo found here offers a rare opportunity to verify this alternative model. In Fig. 2 it can be seen that the prominent giant stellar halo of this BCG is elongated (~80 kpc at position angle ~45 deg). If improved radio imaging of this likely mini-halo reveals an extent and elongation matching that of the BCG stellar halo, which dominates the stellar content of the cluster core region, it would provide the much-needed observational support to this (non-standard) supernova model of radio mini-haloes.

5. Conclusions

We have investigated the sparsely studied galaxy cluster Abell 980 ($z = 0.1582$) by analysing its archival data from GMRT (150 and 325 MHz), EVLA (1.5 GHz), and *Chandra*. The ICM is found to have a quasi-relaxed appearance, with a cool core (ICM with $T \sim 4.2$ keV) of size ~100 kpc, surrounded by a large (~500 kpc) hot gaseous halo ($T \sim 6.8$ keV) with two brightness discontinuities. The rich diversity of this cluster radio emission is found to include (i) two large diffuse sources of the ultra-steep spectrum (USS) located near the opposite extremities of the ICM; (ii) a bright double radio source (~55 kpc) coincident with the BCG and which lies close to the centre of the cool core of the cluster; and (iii) a probable radio mini-halo of average size ~110 kpc associated with the BCG, which itself possesses a huge ellipsoidal stellar halo of size ~80 kpc. All four radio sources may have been created by the BCG at different stages and in different circumstances. The two large diffuse USS sources may be highly aged relics of the radio lobes produced by the BCG during its previous active phase ~260 Myr ago and eventually propelled buoyantly towards the outskirts of the ICM, where they have been found to create the two X-ray discontinuities in the ICM. The bright small double source with a central radio core is a probable outcome of a recent episode of activity in the BCG. Deeper radio imaging of the newly detected mini-halo presents a rare opportunity to verify the recent model in which mini-haloes are explained as aggregate radio emission from Type I supernovae within the stellar population distributed across the cluster core.

References

Baldwin, J. E., & Scott, P. F. 1973, MNRAS, 165, 259
Cavaliere, A., & Fusco-Femiano, R. 1976, A&A, 49, 137
Chambers, K. C., Magnier, E. A., Metcalfe, N., et al. 2016, ArXiv e-prints [arXiv:1612.05560]
Chibueze, J. O., Sakemi, H., Ohmura, T., et al. 2021, Nature, 593, 47
Ebeling, H., Voges, W., Bohringer, H., et al. 1996, MNRAS, 281, 799
Eckert, D., Molendi, S., & Paltani, S. 2011, A&A, 526, A79
Enßlin, T. A., & Gopal-Krishna 2001, A&A, 366, 26
Fujita, Y., Matsumoto, T., & Wada, K. 2004, ApJ, 612, L9
Giacintucci, S., Markevitch, M., Cassano, R., et al. 2019, ApJ, 880, 70
Gitti, M., & Schindler, S. 2004, A&A, 427, L9
Godfrey, L. E. H., Morganti, R., & Brienza, M. 2017, MNRAS, 471, 891
Heinz, S., Churazov, E., Forman, W., Jones, C., & Briel, U. G. 2003, MNRAS, 346, 13
Intema, H. T., Jagannathan, P., Mooley, K. P., & Frail, D. A. 2017, A&A, 598, A78
Jamrozy, M., Klein, U., Mack, K.-H., Gregorini, L., & Parma, P. 2004, A&A, 427, 79
Jamrozy, M., Konar, C., Machalski, J., & Saikia, D. J. 2008, MNRAS, 385, 1286
Kadam, S. K., Sonkamble, S. S., Pawar, P. K., & Patil, M. K. 2019, MNRAS, 484, 4113
Kalberla, P. M. W., Burton, W. B., Hartmann, D., et al. 2005, A&A, 440, 775
Kempner, J. C., & David, L. P. 2004, ApJ, 607, 220
Kim, J.-Y., & Trippe, S. 2014, J. Korean Astron. Soc., 47, 195
Kraft, R. P., Forman, W. R., Churazov, E., et al. 2004, ApJ, 601, 221
Lebedev, V. S., & Lebedeva, I. A. 1991, BSAO, 31, 88
Markevitch, M., & Vikhlinin, A. 2007, Phys. Rep., 443, 1
McNamara, B. R., & Nulsen, P. E. J. 2007, ARA&A, 45, 117
Murgia, M., Govoni, F., Markevitch, M., et al. 2009, A&A, 499, 679
Murgia, M., Parma, P., Mack, K.-H., et al. 2011, A&A, 526, A148
Omar, A. 2019, MNRAS, 484, L141
Paul, S., Salunkhe, S., Sonkamble, S., et al. 2020, A&A, 633, A59
Planck Collaboration XIII. 2016, A&A, 594, A13
Rines, K., Geller, M. J., Diaferio, A., & Kurtz, M. J. 2013, ApJ, 767, 15
Rudnick, L., & Lemmerman, J. A. 2009, ApJ, 697, 1341
Sanders, J. S. 2006, MNRAS, 371, 829
Sansom, A. E., O'Sullivan, E., Forbes, D. A., Proctor, R. N., & Davis, D. S. 2006, MNRAS, 370, 1541
Savini, F., Bonafede, A., Brüggen, M., et al. 2018, MNRAS, 478, 2234
Sbarufatti, B., Treves, A., & Falomo, R. 2005, ApJ, 635, 173
Sohn, J., Geller, M. J., Diaferio, A., & Rines, K. J. 2020, ApJ, 891, 129
Sonkamble, S. S., Vagshette, N. D., Pawar, P. K., & Patil, M. K. 2015, Ap&SS, 359, 21
Turner, R. J. 2018, MNRAS, 476, 2522
van Weeren, R. J., Intema, H. T., Lal, D. V., et al. 2014, ApJ, 786, L17
ZuHone, J. A., Markevitch, M., Brunetti, G., & Giacintucci, S. 2013, ApJ, 762, 78

Appendix A: Radio data

A.1. Spectral index and error computation

GMRT 150 and 325 MHz images are made with uniform weight and appropriate uv-taper using the SPAM pipeline and are convoluted to a beam of size $33'' \times 22''$ and PA $60°$ to make the spectral index map. The masking for this image was taken at the 3σ isophotes of the 325 MHz map.

For the spectral index map between 1.5 GHz and 325 MHz we made the maps using common uv-distance cut and uniform weights for both the frequencies and applied suitable uv-tapers in the uv-plane to get approximately the same resolution. Furthermore, the maps were convoluted to a beam of $10'' \times 10''$ and were masked at the 3σ contour of the 1.5 GHz image.

The computation of the spectral index for both the cases was done using IMMATH task of CASA with the relation

$$\alpha = \frac{\log(S_{\nu_2}/S_{\nu_1})}{\log(\nu_2/\nu_1)}, \tag{A.1}$$

where $S_{\nu_\#}$ and $\nu_\#$ (with $\nu_1 > \nu_2$) are the values of flux density and the frequency of observation, respectively. Spectral index maps between 150 and 325 MHz are shown in Fig. 3, and between 325 MHz and 1.5 GHz in Fig. A.1.

The spectral index error was calculated with the same IMMATH task using the relation (Kim & Trippe 2014)

$$\alpha_{err}(\alpha_{\nu_2,\nu_1}) = \frac{1}{\log(\nu_2/\nu_1)} \times \left[\frac{\sigma^2_{\nu_1}}{I^2_{\nu_1}} + \frac{\sigma^2_{\nu_2}}{I^2_{\nu_2}} \right]^{\frac{1}{2}}, \tag{A.2}$$

where I is the total intensity at respective frequencies at each of the pixels. The error maps (see the inset in Fig. 3) shows a very reliable spectral map.

A.2. Radio emissivity calculation

Physical and morphological radio properties of the radio halo and mini-halo can be studied from their averaged brightness profiles. The emissivity of the radio halo or the mini-halo can be calculated if the central brightness and the e-folding radius are known, which can be obtained by fitting the azimuthally averaged brightness profile with the exponential relation (Murgia et al. 2009)

$$I(r) = I_0 e^{-r/r_e}, \tag{A.3}$$

where the central surface brightness (I_0) and e-folding radius (r_e) are two independent parameters.

Analysis of the mini-halo becomes complicated because of the presence of the central radio galaxy. To separate the contribution of this central source from the mini-halo, the point-source-subtracted image (see §2.1 for image analysis) is used for the emissivity calculation. Concentric annuli of radius 3 arcsec to 30 arcsec are placed on a source spaced by 3 arcsec to get an azimuthally averaged brightness profile. The flux is measured within 3σ (three sigma) region after removing the contribution from source A. The obtained values of $I_0 = 31.5 \pm 2.8$ μJy arcsec^{-1} and $r_e = 41.3 \pm 2.8$ kpc after fitting are used in the following relation to calculate volume-averaged radio emissivity (Murgia et al. 2009):

$$< J > \simeq 7.7 \times 10^{-41} (1+z)^{3+\alpha} \cdot \frac{I_0}{r_e}. \tag{A.4}$$

Here, the units of emissivity, I_0 and r_e are erg s^{-1} cm^{-3} Hz^{-1}, μJy arcsec^{-1} and kpc, respectively. Emissivity for the mini-halo in A980 has been computed to be $1.1 \pm 0.2 \times 10^{-40}$ erg s^{-1} cm^{-3} Hz^{-1}.
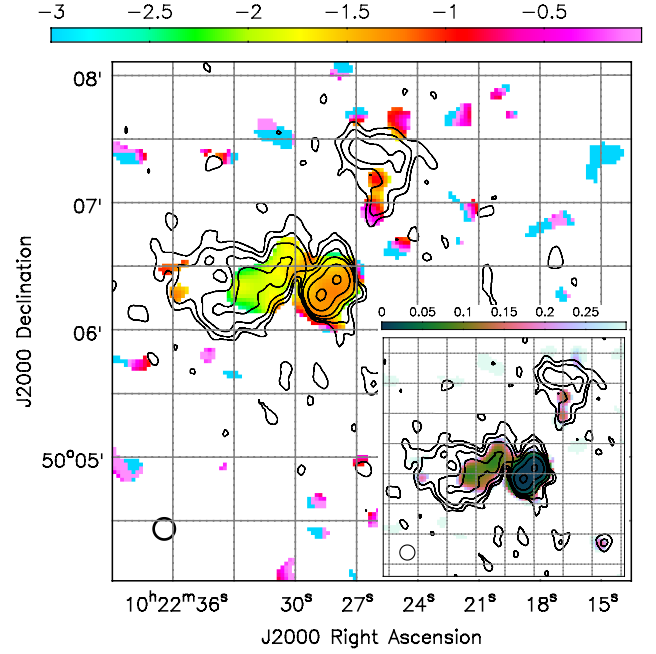

Fig. A.1. spectral index and error maps for the cluster made using GMRT 325 MHz and EVLA L-band map

A.3. Magnetic field and the spectral age

If the break frequency (ν_{br}) and the magnetic field are known, one can obtain the age of the radio emitting electron source using the relation (Jamrozy et al. 2004)

$$\tau = 1.59 \times 10^3 \nu_{br}^{-0.5} \frac{B_{eq}^{0.5}}{B_{eq}^2 + B_{CMB}^2} Myr, \tag{A.5}$$

where B_{eq} is the equipartition field (in μG), $B_{CMB} = 3.25(1+z)^2$ is the magnetic field equivalent to the microwave background, and ν_{br} is the break frequency (in GHz). Here we have assumed the break frequency at the lower end of our observation ($\nu_{br} = 150$ MHz). The equipartition magnetic field is calculated using the usual relation

$$B_{eq} = 7.91 \left[\frac{1+k}{(1+z)^{\alpha-3}} \frac{S_0}{\nu_0^\alpha \theta_x \theta_y s} \frac{\nu_u^{\alpha+\frac{1}{2}} - \nu_l^{\alpha+\frac{1}{2}}}{\alpha + \frac{1}{2}} \right]^{\frac{2}{7}}, \tag{A.6}$$

where S_0 is the flux density (in mJy) at the observing frequency (ν_0), k is the ratio of the energy content in relativistic protons to that of electrons, ν_l and ν_u are the lower and upper integration boundaries for the radio luminosity, s is the path length through the source in the line of sight (in kpc), and θ_x and θ_y are the source extents in two directions (measured in arcsec). For our case we adopted k=1, $\nu_l = 0.01$ GHz, and $\nu_u = 100$ GHz. We used θ_x and θ_y as the size of the sources A and B mentioned in §3.1.1 and the path length, s, assumed to be the same as the average size of these sources.

Appendix B: X-ray data

B.1. Extraction of global X-ray properties

The global X-ray properties of the cluster X-ray emission were determined by extracting a 0.5–8 keV spectrum of the X-ray photons from within a $150''$ (408 kpc) circular region centred on the

Table B.1. Parameters of double β-model

Region	β	r_{c1} (arcmin)	r_{c2} (arcmin)	ratio (R)	norm (10^{-4})	const. (10^{-6})	χ^2/dof
0° - 360°	0.65±0.05	1.10±0.10	0.03±0.01	7.62±4.34	1.88±0.08	2.00±1.0	68.69/72

r_{c1} - outer core radius, r_{c2} - inner core radius, R - ratio of the two β components at radius = 0

Table B.2. Parameters of broken power-law density model

Region	$\alpha1$	$\alpha2$	r_{sh} (arcmin)	n_0 (10^{-4})	Compression (C)	χ^2/dof
10°- 100°	0.62 ± 0.06	1.40 ± 0.41	1.30 ± 0.06	0.50 ± 0.13	1.20 ± 0.12	25.15/32
175°- 243°	0.26 ± 0.17	1.02 ± 0.26	1.32 ± 0.10	0.65 ± 0.16	1.35 ± 0.15	15.63/12

X-ray peak of the cluster. It is well-founded that the X-ray emission from the central giant elliptical galaxy in a cluster or group can significantly contaminate the estimate of ICM temperature near the cluster centre. To verify how far the central BCG in our cluster contaminated our spectral fit, especially in the innermost region, we tried by excluding the central 1, 2, and 3 arcsec and estimated the temperature and monitored the fit quality of the innermost region. We found that the fit with 2 arcsec exclusion provides the best fit with a reduced chi-square of 0.99. In addition, the central 2 arcsec roughly contains 95 per cent of the encircled point-source energy (Sansom et al. 2006). Therefore, we finally excluded the central 2 arcsec region so that the diffuse gas in the innermost region does not get contaminated by the central point source. A corresponding background spectrum was extracted from the normalized blank sky frame, and the appropriate responses were generated. The spectrum was binned such that every energy bin contains at least ~20 counts and was then imported to XSPEC 12.9.1 for fitting adopting the χ^2 statistics. The combined spectrum was fitted with an absorbed single temperature APEC model with the Galactic absorption fixed at $N_H^{Gal} = 9.16 \times 10^{19}$ cm^{-2} (Kalberla et al. 2005), letting the temperature, metallicity, and normalization parameter to vary. The best fit resulted in the minimum $\chi^2 = 219.01$ for 210 degrees of freedom (dof).

B.2. Surface brightness profile

We extracted azimuthal, blank sky background subtracted, exposure corrected surface brightness (SB) profiles from a series of concentric annuli (width = 2 arcsec) centred on the X-ray peak. Here we assumed spherical symmetry of the ICM. We used PROFFIT V 1.5 package[3] (Eckert et al. 2011) to fit the SB profile with a single β-model (Cavaliere & Fusco-Femiano 1976), but it did not fit well in the central region (see Fig. 4 (b)). In this profile, one can clearly see the central brightness excess, which is a typical characteristic of the cool-core system. We therefore added another β component to model the central excess, and the best-fit parameters are shown in Table B.1. The combined model (double β-model) is represented as the blue solid line in Fig. 4 (b). This suggests that A980 is indeed a cool-core cluster.

B.3. Edge characterization

We extracted the surface brightness profile up to a radius of 3′ in the energy range of 0.5–3.0 keV along 10°– 100°and 175°–

243°, and fitted a deprojected broken power-law density model within PROFFIT. The density model is defined as

$$n(r) = \begin{cases} C\,n_0 \left(\frac{r}{r_{\text{front}}}\right)^{-\alpha1}, & \text{if } r \leq r_{\text{front}} \\ n_0 \left(\frac{r}{r_{\text{front}}}\right)^{-\alpha2}, & \text{if } r > r_{\text{front}} \end{cases}, \quad (B.1)$$

where n is the electron number density, n_0 is the density normalization, $C = n_{e_2}/n_{e_1}$ is the density compression factor, $\alpha1$ and $\alpha2$ are the power-law indices, r is the radius from the centre of the sector, and r_{front} is the radius corresponding to the putative front. All the parameters of the model were kept free during the fit. The best-fitting profiles are shown in Fig. 4(c), while the best-fitting parameters are listed in Table B.2. From this profile it is clear that there is a jump in the electron density at ~1.3′ (212 kpc) in both the regions.

Furthermore, we extracted the spectrum from two regions (T_1 and T_2) on either side of the north-west edge and fitted them with a single temperature APEC model by keeping the redshift fixed at 0.1582. The best-fit temperature values for T_1 and T_2 are 5.77±0.48 keV and 10.90±3.33 keV, respectively. The T_1 region contains hot dense gas and a sharper boundary compared with T_2. This indicates that the north-west edge is due to the presence of a cold front. We also extracted the spectra on either side of the south-east edge and fitted them in the same way, yielding best-fit temperatures of 5.53±0.52 keV and 12.22±3.87 keV, respectively. These derived temperature values seem to indicate that the south-east edge is also a cold front. We also obtained pressure for two cold fronts using $p = nkT$, where $n = n_e + n_H$ (i.e. total number density = electron density + hydrogen ion density) satisfies the relation $n_e = 1.2 n_H$. For pressure, we needed the electron density, which was obtained from the best-fit APEC normalization following the method described in Kadam et al. (2019). For the north-west cold front the measured values of pressure across the pre- and post-cold-front regions are $5.38 \pm 0.72 \times 10^{-11}$ erg cm^{-3} and $4.49 \pm 0.40 \times 10^{-11}$ erg cm^{-3}, respectively, whereas the south-east cold front pressure values are $1.03 \pm 0.32 \times 10^{-11}$ erg cm^{-3} and $1.04 \pm 0.10 \times 10^{-11}$ erg cm^{-3}. Therefore, these values suggest that the pressure is nearly continuous in pre- and post-cold-front regions, which agrees with the standard definition of a cold front. However, the temperature measurement contains large uncertainties, and therefore it is hard to arrive at a proper conclusion. Long-exposure X-ray data would be needed to confirm these cold fronts.